



High-throughput electrochemical sensing platform for screening nanomaterial–biomembrane interactions

Cite as: Rev. Sci. Instrum. **91**, 025002 (2020); <https://doi.org/10.1063/1.5131562>

Submitted: 14 October 2019 . Accepted: 23 January 2020 . Published Online: 10 February 2020

Joshua Owen , Maksims Kuznecovs , Raeesa Bhamji, Nicola William, Natalia Domenech-Garcia, Michelle Hesler, Thorsten Knoll, Yvonne Kohl, Andrew Nelson, and Nikil Kapur



View Online



Export Citation



CrossMark

ARTICLES YOU MAY BE INTERESTED IN

[Microwave interferometer for phase and response time measurements](#)

Review of Scientific Instruments **91**, 024707 (2020); <https://doi.org/10.1063/1.5138591>

[Charge breeding at GANIL: Improvements, results, and comparison with the other facilities](#)

Review of Scientific Instruments **91**, 023315 (2020); <https://doi.org/10.1063/1.5128661>

[Developing a camera-based 3D momentum imaging system capable of 1 Mhits/s](#)

Review of Scientific Instruments **91**, 023316 (2020); <https://doi.org/10.1063/1.5138731>



JANIS

Rising LHe costs? Janis has a solution.
Janis' Recirculating Cryocooler eliminates the use of Liquid Helium for "wet" cryogenic systems.

sales@janis.com www.janis.com [Click for more information.](#)

High-throughput electrochemical sensing platform for screening nanomaterial–biomembrane interactions

Cite as: Rev. Sci. Instrum. 91, 025002 (2020); doi: 10.1063/1.5131562

Submitted: 14 October 2019 • Accepted: 23 January 2020 •

Published Online: 10 February 2020



Joshua Owen,^{1,a)} Maksims Kuznecovs,¹ Raeesa Bhamji,² Nicola William,² Natalia Domenech-Garcia,² Michelle Hesler,³ Thorsten Knoll,³ Yvonne Kohl,³ Andrew Nelson,² and Nikil Kapur¹

AFFILIATIONS

¹Institute of Thermofluids, School of Mechanical Engineering, University of Leeds, Leeds LS2 9JT, United Kingdom

²School of Chemistry, University of Leeds, Leeds LS2 9JT, United Kingdom

³Fraunhofer Institute for Biomedical Engineering IBMT, Joseph-von-Fraunhofer-Weg 1, 66280 Sulzbach, Germany

^{a)}Author to whom correspondence should be addressed: J.J.Owen@leeds.ac.uk

ABSTRACT

A high-throughput, automated screening platform has been developed for the assessment of biological membrane damage caused by nanomaterials. Membrane damage is detected using the technique of analyzing capacitance–current peak changes obtained through rapid cyclic voltammetry measurements of a phospholipid self-assembled monolayer formed on a mercury film deposited onto a microfabricated platinum electrode after the interaction of a biomembrane-active species. To significantly improve wider usability of the screening technique, a compact, high-throughput screening platform was designed, integrating the monolayer-supporting microfabricated electrode into a microfluidic flow cell, with bespoke pumps used for precise, automated control of fluid flow. Chlorpromazine, a tricyclic antidepressant, and a citrate-coated 50 nm diameter gold nanomaterial (AuNM) were screened to successfully demonstrate the platform's viability for high-throughput screening. Chlorpromazine and the AuNM showed interactions with a 1,2-dioleoyl-*sn*-glycero-3-phosphocholine (DOPC) monolayer at concentrations in excess of 1 $\mu\text{mol dm}^{-3}$. Biological validity of the electrochemically measured interaction of chlorpromazine with DOPC monolayers was confirmed through quantitative comparisons with HepG2 and A549 cytotoxicity assays. The platform also demonstrated desirable performance for high-throughput screening, with membrane interactions detected in <6 min per assay. Automation contributed to this significantly by reducing the required operating skill level when using the technique and minimizing fluid consumption.

Published under license by AIP Publishing. <https://doi.org/10.1063/1.5131562>

I. INTRODUCTION

Advances in nanotechnology have resulted in widespread usage of nanomaterials, often with applications in consumer products, biomedical technologies, and sensing technologies.^{1–4} However, toxicity hazards associated with nanomaterials have been widely reported, with growing research in the field of nanotoxicology emphasizing the need for screening techniques to characterize nanomaterial hazards.^{5–12} As the applications for engineered nanomaterials continue to grow, high-throughput, *in vitro* screening solutions are essential to accelerate the process of evaluating the toxicity of novel engineered nanomaterials and to meet the demand for hazard identification.^{13,14} High-throughput *in vitro* toxicity sensing

technologies also provide an alternative to *in vivo* animal toxicity studies, which have ethical implications and are not economically feasible for screening a vast range of nanomaterials.^{3,15,16}

Understanding cytotoxicity remains a particularly important and significant challenge in the field of nanotoxicology, as nanomaterials, due to their small size, can have unique properties that influence the mechanisms of interaction with cell membranes.¹⁷ Engineered nanomaterials can interact with cell membranes through adsorption onto the membrane, penetration through the membrane, and endocytosis.^{17–21} The understanding of nanomaterial cytotoxicity is challenging due to the complexity of cell membranes and the wide range of nanomaterial parameters, such as particle size, material, and shape, that can influence the mechanisms of membrane

interaction.^{5,7,10,11,17,21} Cell-based *in vitro* toxicity assays are typically employed for the assessment of nanomaterial cytotoxicity, which are adapted for high-throughput screening through the use of high quantity multi-well plate platforms.^{22–24} However, generally there remains a lack of high-throughput techniques for *in vitro* assessment of nanomaterial hazards.

One solution to rapid screening of the interaction of the nanomaterial with biological membranes is the application of a membrane-on-chip sensing technique, one of which measures an electrochemical response to detect interaction with a phospholipid, self-assembled monolayer supported on a mercury (Hg) electrode.^{25–35} This has been well-established as an effective technique for quantifying and mechanistically understanding biomembrane interaction. The interaction with the monolayer is evaluated through highly sensitive and rapidly detectable changes in capacitance–current peaks after the interaction of a biomembrane-active compound or particle with the Hg-supported monolayer, measured through the application of rapid cyclic voltammetry (RCV). A strong correlation exists between biomembrane interaction measured using the monolayer technique and physical membrane damage of a more complex biological bilayer membrane, confirmed through direct comparison with phospholipid unilamellar vesicle studies.^{21,36}

Recently, the technique has been improved through the use of a microfabricated electrode, consisting of platinum (Pt) disks on to which Hg can be deposited to support the phospholipid monolayer,^{25,26} as opposed to a hanging Hg drop electrode used in original studies by Nelson,²⁸ enabling safe and robust use of Hg as a working electrode (WE) in a flow environment. Another significant advantage of this is that the phospholipid monolayer can be rapidly re-established after measurement to create a reusable electrode, ideal for high-throughput screening. This is advantageous compared to other high-throughput *in vitro* methods, such as high quantity, multi-well plate cell-based assays, which require a longer time period to obtain meaningful results.^{14,23} This also reduces the possibility of nanomaterial transformations (e.g., aggregation) during assessment, which have been reported to contribute to ambiguity in cell assay studies.^{37–39} However, despite robust characterization and

validation of the sensing technique,⁴⁰ limitations still exist, such as a complex operating procedure and excessive fluid consumption, preventing its wider adoption for high-throughput hazard assessment of nanomaterials.

With advances in microfluidic flow cell technology and the possibility to automate processes, significant potential exists to improve the current screening methodology, as most recently described by Vakurov *et al.*,⁷ to reduce fluid consumption, increase throughput, and improve usability. Microfluidic flow cells offer significant benefits for high-throughput biosensing applications, by reducing fluid consumption in a low cost and easy to manufacture, high precision cell.^{41–47} The application of microfluidic technology is particularly advantageous for nanomaterial toxicity screening, enabling consistent transport of the nanomaterial in high precision laminar fluid flow and being well-suited for automation.¹⁶ Automation of the sensing technique also offers the potential to reduce the required operator skill level by simplifying the screening process.

This study details the development of a new automated screening platform, incorporating a microfluidic flow cell, containing an Hg-supported membrane monolayer, for high-throughput sensing of nanomaterial–biomembrane interactions. The new screening platform offers a significant enhancement on the previous generations of the biomembrane-sensing system to create a rapid, high-throughput sensor viable for *in vitro* screening of nanomaterial–membrane interaction, decreasing required operator skill levels and decreasing fluid consumption. A gold nanomaterial (AuNM) and chlorpromazine, a pharmaceutical compound, were screened using the screening platform to demonstrate its viability as a high-throughput sensor for assessing biomembrane interactions of the nanomaterial and to prove equivalence to well-validated studies using the sensing technique.

II. AUTOMATED SCREENING PLATFORM DESIGN

A. Overview of the screening technique

A schematic of the sensing technique is provided in Fig. 1 to demonstrate how biomembrane activity is assessed through

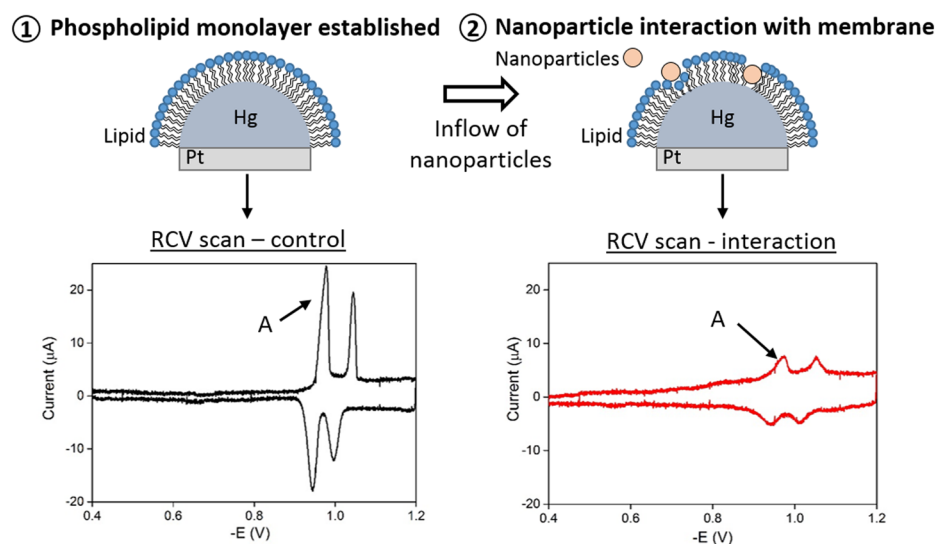


FIG. 1. Schematic of the screening technique to evaluate biomembrane interaction of the nanomaterial with an Hg-supported phospholipid membrane monolayer through analysis of a RCV response, with peak “A” highlighting the capacitance–current peak used to provide a quantitative comparison of biomembrane interaction.

RCV analysis. After supporting the phospholipid monolayer onto a Hg electrode, the characteristic RCV response consists of two capacitance–current peaks on the forward and reverse scans when the phospholipid 1,2-dioleoyl-*sn*-glycero-3-phosphocholine (DOPC) is used.⁴⁰ A biomembrane-active species (e.g., nanoparticles) can adsorb to and/or penetrate the monolayer, during flow across the coated electrode, suppressing the capacitance–current and/or shifting the potential of peaks measured using RCV. The first capacitance–current peak on the forward scan, labeled “A” in Fig. 1, is often of significant interest to the operator and this peak is used to provide a quantitative indication of a species interaction with the monolayer. The capacitance–current peak represents a monolayer phase change corresponding to ingress of electrolyte into the phospholipid monolayer.^{28,40}

The aim of the automated platform design was to utilize this well-established sensing technique and create an easy-to-use, high-throughput, *in vitro* sensing platform for rapid screening of nanomaterials. A critical analysis of the previous state of the technology (the methodology as described by Vakurov *et al.*⁷) was completed to identify limitations of the method, leading to the following objectives being set as criteria for the screening platform design. These objectives will enable wider potential use of the technique for assessment of nanomaterial hazards:

- The screening process was to be automated, thus significantly decreasing the complexity of the screening procedure and improving repeatability of the system to enable an inexperienced operator to use the screening system reliably and with minimal guidance.
- The time required to screen nanomaterials was to be reduced, thus improving throughput and enhancing the feasibility of the technique for screening vast quantities of nanomaterials.
- The screening platform was to be compactly designed, avoiding the use of large and numerous components to reduce space requirements and enable the device to be portable, improving feasibility of the design as a single screening platform.
- A graphical user interface was to be developed to simplify control of the system, making the system easy-to-use for inexperienced operators, requiring minimal control to complete

the screening process and therefore contributing to improved throughput.

- Fluid consumption and waste was to be reduced by optimizing flow rates and volumes consumed through automation and reducing tubing usage to make the technique more viable for screening vast quantities of the nanomaterial.

The newly-developed automated screening platform is shown in Fig. 2, consisting of a microfluidic flow cell containing the phospholipid monolayer supported on a Hg sensing electrode, four automated bespoke syringe pumps enabling storage and transportation of fluids (electrolyte, test sample, phospholipid, and water) into the flow cell, a field-programmable gate array (FPGA) data acquisition and control unit used to interface between software and hardware and an ACM Research Potentiostat for electrochemical measurements. A laptop was connected to control the screening platform, interfacing with syringe pumps and the FPGA control unit. The components of the platform are discussed in more detail in the following sections.

B. Microfluidic flow cell and the sensing electrode

A microfluidic flow cell was designed to transport fluids consumed in the screening process to the sensing electrode, contained within the flow cell, for electrochemical analysis. A layered approach was used for the microfluidic flow cell design, with flow cell layers fabricated using a laser cutter. This allows an inherently 3D structure to be established with the ability to seal ancillary components into the flow cell. Cast poly(methyl methacrylate) (PMMA) was employed for harder layers of the flow cell and a Pt-cured silicone sheet was used for softer layers. The flow cell components were fastened together using bolts to provide a compression seal between softer and harder layers to prevent leakage of fluids and enable electrochemical measurements, by isolating electrical connections from contact with electrolyte. The design is both robust and provides excellent sealing.

The microfluidic flow cell is shown in Fig. 3. The main components of the design include (1) a ceramic junction screw-type silver/silver chloride (Ag/AgCl) reference electrode (RE) containing 3M NaCl gel (ALS); (2, 5, and 8) PMMA layers; (3) a 25 mm

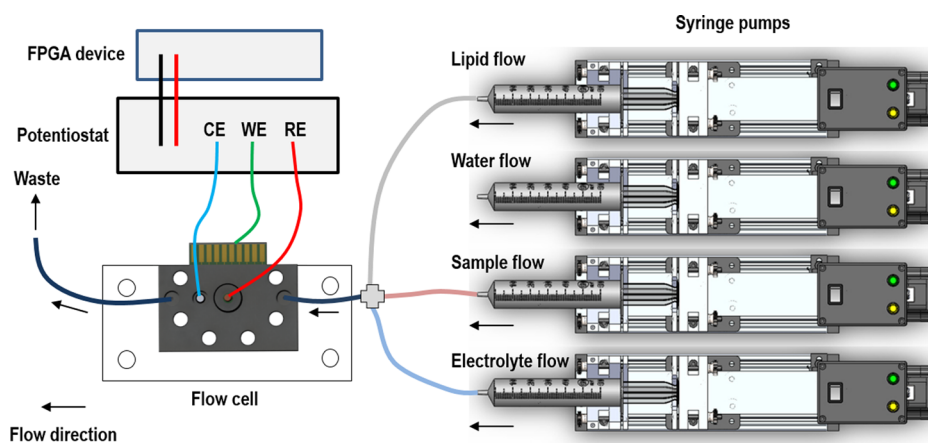


FIG. 2. Automated platform used for electrochemical analysis of biomembrane activity of compounds and particles after interaction with an Hg-supported phospholipid monolayer, consisting of a microfluidic flow cell, four syringe pumps, an FPGA data acquisition and control unit, and a potentiostat, where RE is the reference electrode, CE is the counter electrode, and WE is the working electrode.

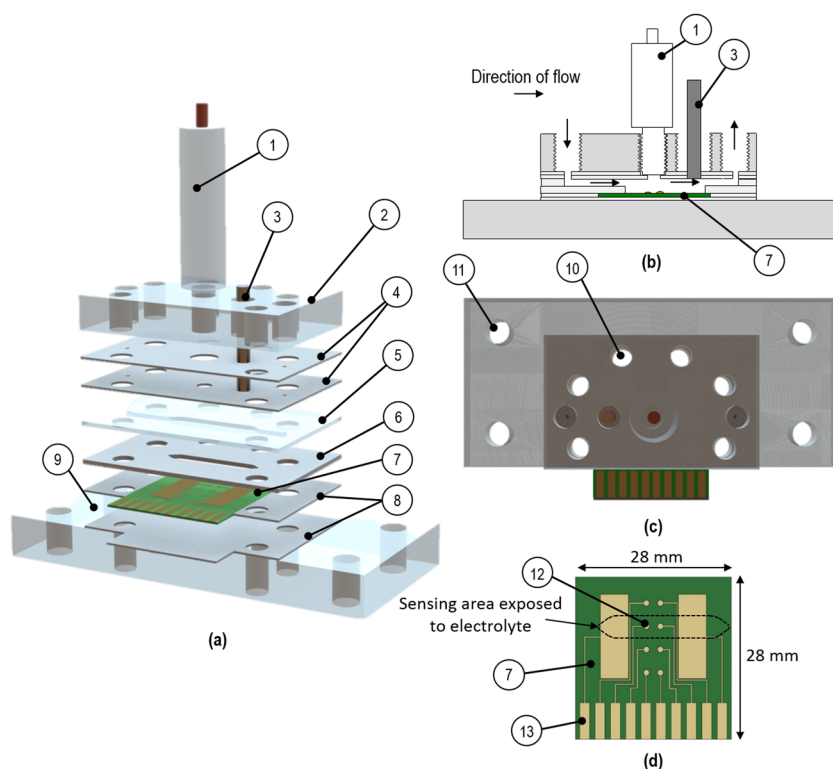


FIG. 3. Microfluidic flow cell showing (a) exploded assembly of components, (b) cross-section schematic of the flow cell, (c) top view of the flow cell assembly, and (d) microfabricated sensing Pt/Hg electrode, consisting of (1) Ag/AgCl reference electrode, (2) PMMA top plate, (3) Pt rod counter electrode, (4) silicone fluid inlet/outlet layers, (5) PMMA flow channel layer, (6) silicone sensing layer, (7) microfabricated sensing Pt/Hg electrode, (8) silicone layers for electrode support and sealing, (9) PMMA bottom plate, (10) screw holes $\times 6$ to mount and seal flow cell, (11) screw holes $\times 4$ to mount sealed flow cell on aluminum breadboard, (12) Pt working electrode, and (13) electrical contacts, sealed from the electrolyte, for potentiostat connection.

long Pt rod with 3.0 mm diameter (Goodfellow), used as the counter electrode, mounted in the flow cell downstream of the working electrode using a flangeless nut and ferrule; (4, 6, and 8) silicone layers to channel fluids through the flow cell and/or seal the flow cell, and (7) a microfabricated Pt/Hg sensing electrode (supplied by Tyn-dall National Institute, Ireland). The Pt/Hg electrode consisted of eight Pt disks (12), with radii of 0.48 mm (of which two disks were deposited with Hg prior to insertion in the flow cell). Silicon nitride-insulated electrical contacts enabled potentiostat connection to the Pt/Hg electrode (13).

Fluids were transported into and out of the flow cell with a 1/16" inner diameter, 1/8" outer diameter, fluorinated ethylene propylene (FEP) tubing mounted in the inlet and outlet ports on the flow cell (layer 2) through the use of standard fittings [1/4"-28 Unified National Fine (UNF) flangeless threaded nuts]. FEP tubing was used for chemical resistance and compatibility with test compounds and particles to prevent contamination. Fluids were transported out of the flow cell and into a waste container. Syringes containing test fluids were connected to tubing via a two-way shut off valve, closed to prevent air bubbles from entering the system when replacing syringes. The tubing from each syringe was connected to a polyether ether ketone cross component to mix fluids prior to the flow cell inlet.

Nanomaterial transport through microfluidic flow cells provides an additional design challenge, with some microfluidic devices reported to have been ineffective at transporting nanomaterials to sensing areas and cell assay well plates.⁴⁷ Challenges with the microfluidic design for nanomaterial transport include ensuring no

aggregation, minimizing entrapment, preventing air bubbles, and decreasing sedimentation of the nanomaterial in fluid tubing.¹⁶ Aggregation and sedimentation of nanomaterials was minimized by using short tubing lengths. The nanomaterial was mixed with electrolyte flow just prior to the flow cell inlet, rather than further upstream, to minimize the possibility of aggregation. Measurements were completed in continuous flow, also decreasing potential time for aggregation of the nanomaterial. Entrapment of the nanomaterial was not observed as a result of minimizing the number of components in the fluid flow path. Although appearing mechanically complex, from a flow perspective, the flow channel within the flow cell is simple. Critically, the dead spaces around ancillary components (e.g., the reference and counter electrodes and piping connections) were minimal reducing the chance of entrapment of the nanomaterial and therefore reducing demand in cleaning between subsequent measurements. The nanomaterial was easily flushed through and removed from the system during cleaning, confirmed by the RCV response.

To confirm that the flow cell effectively transported species to the sensing electrode, as highlighted in Fig. 3, and to confirm that no undesirable flow conditions (such as flow recirculation as the flow channel width expands^{48,49}) influenced transport to the sensing electrode, computational fluid dynamics (CFD) simulations using COMSOL Multiphysics 5.3a⁵⁰ were completed to predict species transport through the flow channel after solving a finite element discretization of the Navier–Stokes equations for laminar fluid. Full details of the methodology used to complete these simulations are provided in the [supplementary material](#).

C. User control interface

An easy-to-use graphical user interface, shown in the [supplementary material](#), was developed in LabVIEW to enable operator control of the screening platform and to display relevant information to the operator. The user interface consisted of operator controls to specify the size of the syringe used and the volume of fluid contained in the syringe for electrolyte, lipid, screening test sample, and water; operator controls to specify the fluid flow rates and potentials for RCV measurements, and the RCV response from which data could be easily extracted. An FPGA data acquisition and control unit controlled the potentials applied by the potentiostat, as determined by the operator on the user interface, and acquired the resulting electrochemical data, presented on the user interface. This enabled the operator to screen nanomaterials with minimal effort, switching between the different processes of the screening procedure with ease, significantly reducing the time required to complete a screening program.

III. EXPERIMENTAL

A. Materials

The AuNM and chlorpromazine were screened to assess interaction with the Hg-supported phospholipid monolayer. The phospholipid used was DOPC, a common component of biological membranes, purchased as 99% pure (Avanti Polar Lipids Alabaster, AL). A minimum dispersion of 0.5 mmol dm^{-3} of DOPC with Milli-Q water ($18.2 \text{ M}\Omega$) was prepared and mixed by gently shaking. The control electrolyte was 0.1 mol dm^{-3} KCl (calcined at 600°C for 2 h) and buffered at pH 7.4 with 0.01 mol dm^{-3} phosphate (phosphate buffered saline or PBS, referred to as “Buffer” on the screening platform control interface).

Chlorpromazine (Sigma-Aldrich), a tricyclic antidepressant with the compound molecular structure shown in the [supplementary material](#), has been regularly screened and shown to be highly biomembrane-active in the previous studies using the RCV phospholipid monolayer membrane-on-chip technique.^{25,26} Therefore, interactions of chlorpromazine with the monolayer were assessed to confirm the validity of the results measured using the new platform at concentrations ranging from 10^{-5} to $10^4 \text{ }\mu\text{mol dm}^{-3}$. Chlorpromazine was also used for comparison with cytotoxicity assays to confirm biological relevance of the electrochemically measured membrane interactions through cell viability studies.

Dispersions of the citrate-coated AuNM (Alfa Aesar) with a diameter of 50 nm were screened in a concentration range from 10^{-3} to $10^2 \text{ }\mu\text{mol dm}^{-3}$ to evaluate the RCV response after interaction with the Hg-supported DOPC monolayer and to demonstrate the performance of the platform as a viable solution to high-throughput *in vitro* screening of nanomaterials. AuNMs have been shown, in some cases, to be cytotoxic, potentially as a result of cell membrane penetration^{11,51} and therefore were chosen to be investigated in this study to demonstrate interaction with a DOPC membrane. The dispersion of the AuNM was reported as a concentration of $\mu\text{mol dm}^{-3}$ of Au in the dispersion, confirmed by inductively coupled plasma mass spectrometry (PerkinElmer SCIEX ELAN DRC-e with a PerkinElmer S10 auto sampler) after digestion of known volumes of the AuNM, from the citrate-coated AuNM stock dispersion, in aqua regia. By determining elemental concentration of

Au using this technique, the appropriate volume of the AuNM was dispersed in Milli-Q water to achieve the Au concentrations reported.

The size of the AuNM was confirmed using dynamic light scattering (DLS) measurements on a Malvern Instruments nanoZS Zeta-sizer prior to the test by dispersing the AuNM in a Milli-Q water medium, showing an average particle diameter of 68 nm, based on intensity plots vs particle diameter in [Fig. 4](#). To confirm that aggregation of the AuNM would not be significant after the dispersion mixed with PBS during flow through the flow cell, the AuNM was dispersed in PBS and DLS measurements were completed after 5 min and 20 min of incubation, with all the AuNM expected to flow through the flow cell within 1 min of mixing with PBS during screening tests. No aggregation was measured during that period, as shown in [Fig. 4](#) by equivalent size distribution observed between the AuNM samples. A scanning electron microscope (SEM) was used to image the AuNM, showing the approximate size and shape of the AuNM used in the study in [Fig. 4](#). Images were obtained by drying an AuNM dispersion on an SEM stub and using an FEI Nova NanoSEM 450 at an operating voltage of 5 kV in the concentric back scattering mode.

To prepare the microfabricated electrode, prior to insertion in the flow cell, it was cleaned in Piranha solution for approximately 15 min, rinsed with Milli-Q water and dried. After cleaning, Hg was deposited onto two Pt bases prior to mounting in the flow cell. Once contained within the flow cell, an RCV potential excursion from -0.4 V to -3.0 V at a scan rate of 100 V s^{-1} was completed, for approximately 30 min, maintained under PBS throughout this period under static conditions to ensure robust adhesion of Hg to the Pt substrate was achieved and any organic material from the Hg surface was removed. A more detailed method for preparation of the microfabricated Pt/Hg electrode is provided by Rashid *et al.*³²

B. Screening methodology—Automated platform

The fluids used during the screening procedure (PBS, DOPC, and sample) were prepared prior to testing by bubbling with argon gas, for a minimum period of 30 min prior to screening, to exclude dissolved oxygen (O_2) in the fluids. After excluding O_2 , individual syringes were filled, mounted on the platform, and connected to the tubing. RCV scans were completed by applying potential excursions between two potentials at a specified scan rate, depending on the stage of the screening procedure. The four stages, controlled from the user interface as shown in the [supplementary material](#), consisted of an “Idle,” “Clean,” “Lipid,” and “Sample” stage.

1. Idle response

During the “Idle” stage, a potential excursion from -0.4 V to -1.2 V was completed at a scan rate of 40 V s^{-1} under static conditions so that the RCV response could be analyzed after each stage of the process. No fluid was flushed into the flow cell during this stage to allow for analysis of the RCV response. An appropriate control RCV response, prior to sample injection, could be confirmed by the operator and the resulting change in the RCV response after the sample was injected could be analyzed. Data were exported from the “Idle” stage, where RCV responses were exported for further analysis.

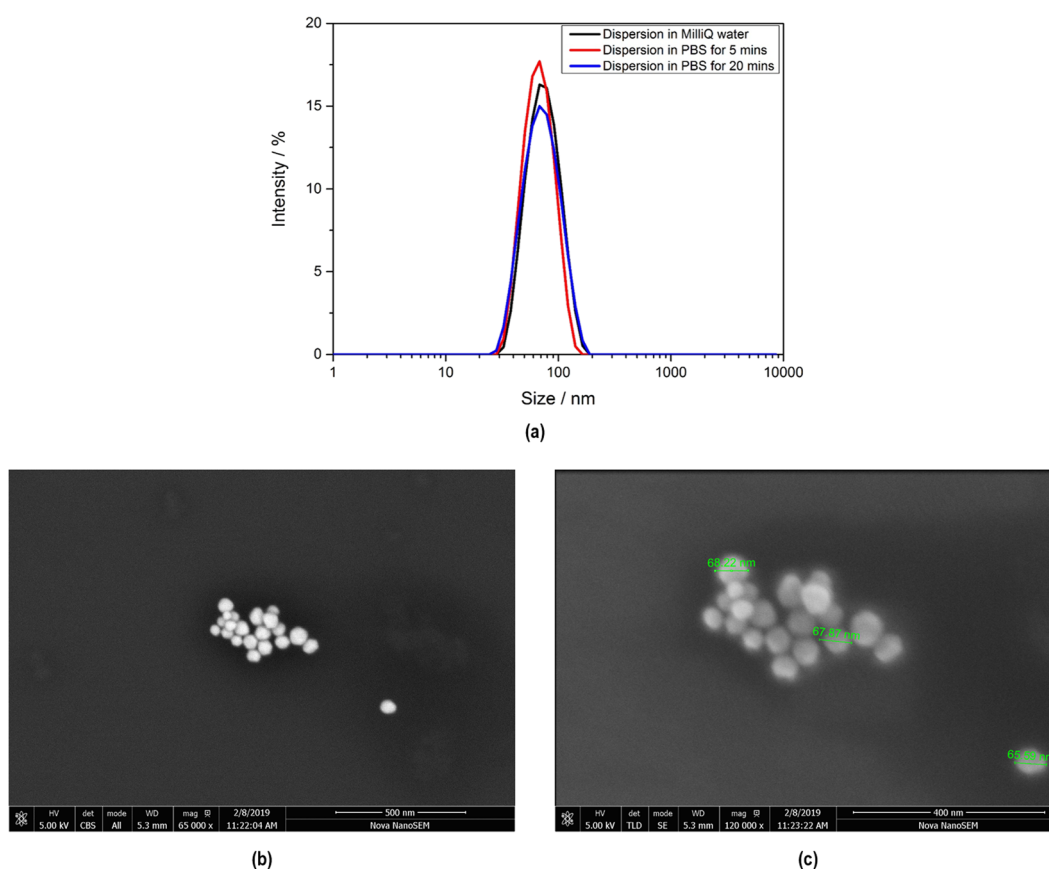


FIG. 4. (a) Intensity plot from DLS measurements of particle size distribution for AuNM dispersions in Milli-Q water and PBS, showing average particle diameter of 68 nm and no aggregation within 20 min in PBS (where time in min is the time at the end of completed measurements), (b) an SEM image of the size distribution of the AuNM, and (c) a higher magnification SEM image showing the approximate size of the AuNM used in the study.

2. Flow cell clean

During the “Clean” stage, a potential excursion of -0.4 V to -3.0 V was completed at a scan rate of 100 V s^{-1} under PBS flow at a constant flow rate of $4.0 \text{ cm}^3 \text{ min}^{-1}$ to flush any remaining sample (and other contaminants) out of the flow cell into a waste container. A minimum of 5 cm^3 of buffer was used to clean the flow cell after each measurement.

3. Supporting a phospholipid membrane monolayer on Hg

Once cleaned, DOPC was flushed into the flow cell at a flow rate of $1.0 \text{ cm}^3 \text{ min}^{-1}$ in the “Lipid” stage. A potential excursion of -0.4 V to -3.0 V was completed at a scan rate of 100 V s^{-1} under PBS flow at a constant flow rate of $4.0 \text{ cm}^3 \text{ min}^{-1}$, before returning to the “Idle” stage to assess the RCV response. A total of 0.5 cm^3 of DOPC was injected to create a stable monolayer on the Hg electrode, confirmed through analysis of the RCV response showing the characteristic peaks, specific to the phospholipid in use, at appropriate potentials.²⁵

4. Sample interaction with the phospholipid membrane monolayer

To assess interaction with the DOPC layer, a test sample was flushed in during the “Sample” stage at a flow rate of $1.0 \text{ cm}^3 \text{ min}^{-1}$ with PBS at a flow rate of $4.0 \text{ cm}^3 \text{ min}^{-1}$. A potential excursion from -0.4 V to -1.2 V was completed at a scan rate of 40 V s^{-1} , similarly to the “Idle” stage, to observe how the peaks changed in real-time during flow of the sample through the flow cell. All sample concentrations were screened three times by evaluating samples in the order of increasing concentration, starting with the lowest concentration. Another three repeats were completed by screening samples in a random order, to ensure that the results were not influenced by the order in which sample concentrations were screened.

After completing a measurement, the syringe containing the test sample was cleaned with MilliQ water (or replaced if a significant interaction was observed). A total of 2 cm^3 of PBS was also injected through the tubing connected to the sample syringe to flush any remaining sample through the tubing into the waste container. The PBS, DOPC, and sample syringes were replaced after all sample concentrations were screened, prior to completing repeat

measurements. The flow cell was then cleaned by selecting the “Clean” process on the user interface to remove any remaining DOPC on the Pt/Hg electrode and flush out the sample, re-establishing the Pt/Hg electrode as a clean sensor available for the next measurement.

C. Screening methodology—Predecessor system

A comparison was made with the well-validated predecessor membrane-on-chip sensor by screening the same samples on both systems. A detailed description of the system and methodology for its use is provided by Vakurov *et al.*⁷ Sample preparation was completed using the same methodology and the screening process was completed in the same order as for the automated platform using an identical electrochemical procedure. PBS was stored in a 0.5 dm³ reservoir on the manual system and transported to the flow cell using a peristaltic pump to maintain a flow rate of 4.67 cm³ min^{−1}. The total volume flow of PBS used to screen the compounds could not be precisely controlled. DOPC and samples were injected into the PBS flow manually using a syringe, upstream of the flow cell. For this reason, flow rates of DOPC and sample were not controlled and volumes of fluid flushed through the cell were not precisely known or consistent for all measurements. For electrochemical measurements, a Ag/AgCl 3.5 mol dm^{−3} KCl reference electrode was fitted into the flow cell. The counter electrode on the microfabricated electrode was used, with a much greater electrode area exposed in the manual system flow cell, due to a different flow cell design. An Autolab PGSTAT12 potentiostat was used for electrochemical measurements.

D. Cytotoxicity assays

To confirm equivalence between the automated RCV platform and well-established *in vitro* techniques, cell viability assays were performed with two widely used cell lines: HepG2 (human hepatocellular carcinoma cells) and A549 (alveolar epithelial cells), both purchased from Leibniz-Institut DSMZ-Deutsche Sammlung von Mikroorganismen und Zellkulturen GmbH (cell line no. ACC-180 and ACC-107, Braunschweig, Germany). Both cell lines were cultured in Roswell Park Memorial Institute medium (RPMI1640, R8758, Sigma-Aldrich, Germany) supplemented with 10% v/v fetal bovine serum (FBS, 26140-079 ThermoFisher Scientific, Germany), 100 U/ml penicillin, and 100 µg/ml streptomycin (5070-63, ThermoFisher Scientific, Germany) in a humidified incubator at 37 °C with 5% CO₂ atmosphere. For the exposure with chlorpromazine, the cells were seeded at a density of 10 000 cells per well in a 96 well plate and cultured for 24 h. The stock solution of chlorpromazine was freshly prepared for all experiments and diluted at the desired concentration in a cell culture medium. The cell culture medium without chemical was used as negative control. The cells were exposed with chlorpromazine in doses ranging from 5 µmol dm^{−3} to 100 µmol dm^{−3} for 24 h. The cell viability reagent alamarBlue (Invitrogen, Germany) was diluted 1:10 in the fresh culture medium and incubated with the cells for 1 h at 37 °C. The fluorescence (excitation 530 nm and emission 590 nm) was determined and the values were blank corrected. The viability of the control cells was set to 100%. Three independent experiments were performed with each cell line and at least three single wells per test condition.

IV. RESULTS AND DISCUSSION

A. Simulation of species transport in the flow cell

The transport of chlorpromazine through the flow cell at a constant flow rate of 4.0 cm³ min^{−1} is shown in Fig. 5, represented by the concentration (*c*) along the bottom surface, relative to the inflow concentration (*c_{in}*) to confirm appropriate transport of the species to the sensing electrode. The average concentration of chlorpromazine over the approximate surface area of the electrodes on the Pt/Hg electrode was determined from the predictions and shown in Fig. 5. The error bars plotted in Fig. 5 represent the maximum and minimum concentrations predicted over the surface area of the electrode at a particular time. A concentration at the electrode equal to the desired inflow concentration (*c/c_{in}* = 1.0) was achieved within approximately 15 s of flow through the flow cell, showing that the flow cell design was effective.

B. Chlorpromazine

The RCV scans for chlorpromazine interactions (red line) measured using the new automated platform are shown in Fig. 6 and are compared against the DOPC baseline (black line) response. The scans for all concentrations are given in the [supplementary material](#). No significant interaction between chlorpromazine and DOPC was observed at low concentrations, but at concentrations above 1 µmol dm^{−3}, a significant interaction was measured. The interactions caused suppression of the capacitance–current peaks, measured between potentials of −0.95 V and −1.05 V, which, at high concentrations, were completely suppressed. Suppression of the capacitance–current peaks after an interaction is typically caused by adsorption onto the DOPC monolayer, influencing the fluidity of the phospholipid layer.¹⁰

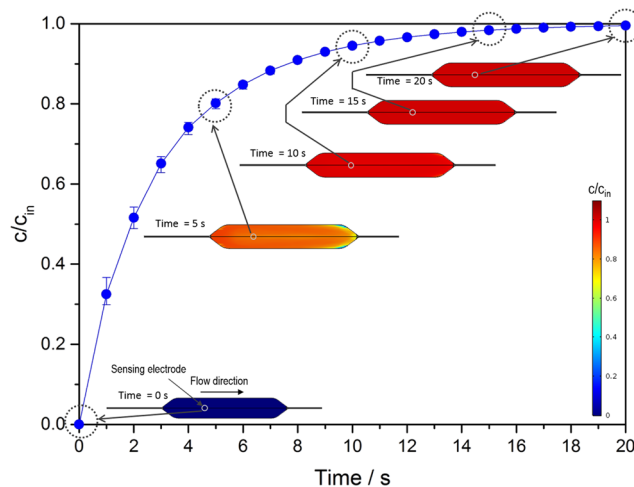


FIG. 5. CFD simulations of time-dependent transport through the flow cell, showing the concentration (*c*) on the bottom of surface of the flow cell (i.e., the location of the electrode), relative to the inflow concentration (*c_{in}*) of chlorpromazine under steady state flow through the flow cell at a flow rate of 4.0 cm³ min^{−1} and showing the average concentration over the surface area of the electrode positioned 17.6 mm from the flow inlet.

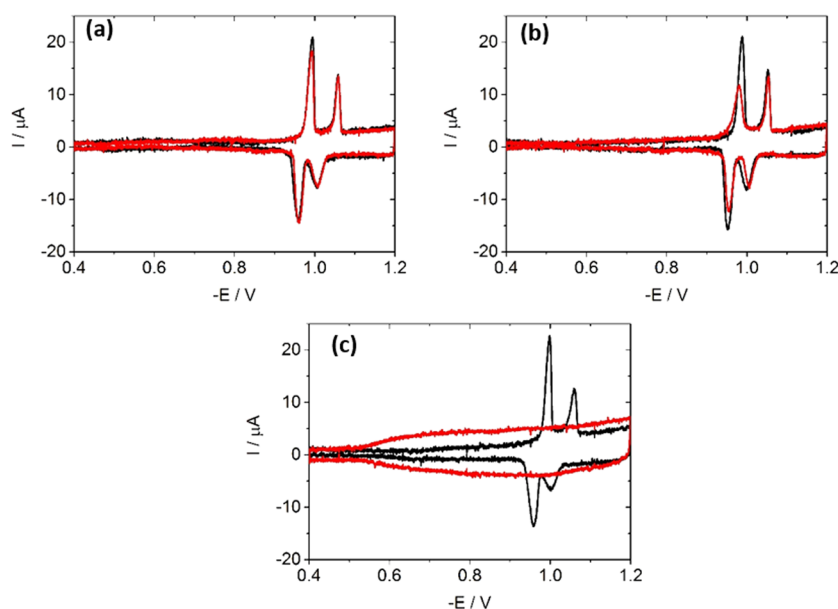


FIG. 6. RCV scans, measured using the automated screening platform at a scan rate of 40 V s^{-1} , of an Hg-supported DOPC monolayer (black line) and interaction with chlorpromazine (red line) in concentrations of (a) $10^{-5} \mu\text{mol dm}^{-3}$, (b) $10 \mu\text{mol dm}^{-3}$, and (c) $10^4 \mu\text{mol dm}^{-3}$ in PBS at pH 7.4 (all RCV scans in the [supplementary material](#)).

The influence of chlorpromazine concentration on the first measured capacitance–current peak height (the peak labeled peak A in Fig. 1 and shown in the forward scans in Fig. 6 at potentials of -0.96 V) is shown in Fig. 7, recorded as a suppression of the peak after interaction with chlorpromazine, relative to an average baseline peak height measured for a stable DOPC monolayer. The average height of the capacitance–current peak of the DOPC monolayer was $19.5 \mu\text{A}$ with a standard deviation of $\pm 1.4 \mu\text{A}$, based on 30

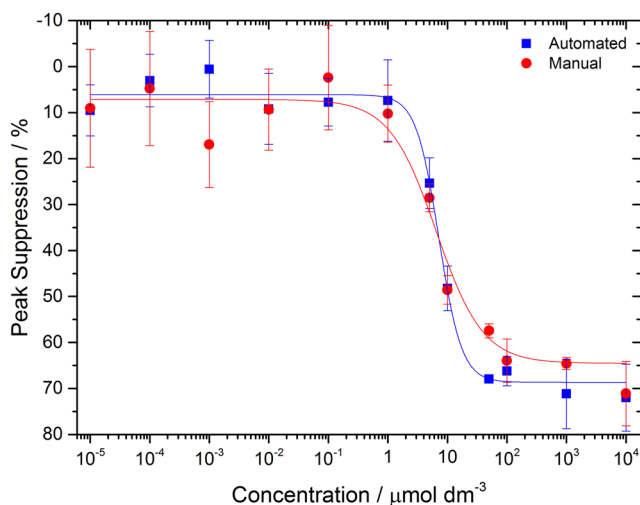


FIG. 7. Percentage suppression of the first capacitance–current peak observed on the forward scan of RCV measurements, at a potential of approximately -0.96 V , after interaction of chlorpromazine at different concentrations with an Hg-supported DOPC monolayer in PBS at pH 7.4, showing equivalence between the new automated platform and the manual predecessor biomembrane sensing system.

measurements of the RCV response. The average percentage peak suppression is shown in Fig. 7 from six measurements of chlorpromazine interaction for each concentration, with error bars representing the standard deviation. The results were compared by screening chlorpromazine using the well-validated manual system to demonstrate equivalence with the automated platform. The average height of the capacitance–current peaks of the DOPC monolayer obtained using the manual system was $20.9 \mu\text{A} \pm 1.5 \mu\text{A}$, similarly determined from an average of 30 measurements. An average of three measurements is shown for the chlorpromazine concentrations screened on the manual system, with error bars representing the standard deviation. More measurements were completed using the new automated platform to demonstrate repeatability, robustness, and durability of the newly designed platform. The average difference between peak suppression measured on the automated and manual system for all concentrations was 4%.

The automated platform dose response curve was compared with *in vitro* cell viability studies in HepG2 and A549 cells in Fig. 8. The comparison was made over the range of concentrations from where the peak suppression became statistically significant to the maximum possible interaction ($5 \mu\text{mol dm}^{-3}$ – $100 \mu\text{mol dm}^{-3}$). RCV peak suppression was normalized against the average maximum peak suppression recorded at $10\,000 \mu\text{mol dm}^{-3}$ in Fig. 7 (72%), to enable direct comparison with the cell viability studies (reported in a measurement range from 0% to 100%). Error bars for the cell viability studies show the standard deviation from three measurements.

A logistic function sigmoidal fit was used for both datasets in Figs. 7 and 8, as defined by the following equation, a fitting typically used for dose response analysis, fitted with the Levenberg Marquardt algorithm:⁵²

$$h = h_{\infty} + \frac{(h_0 - h_{\infty})}{1 + \left(\frac{c}{EC_{50}}\right)^n}, \quad (1)$$

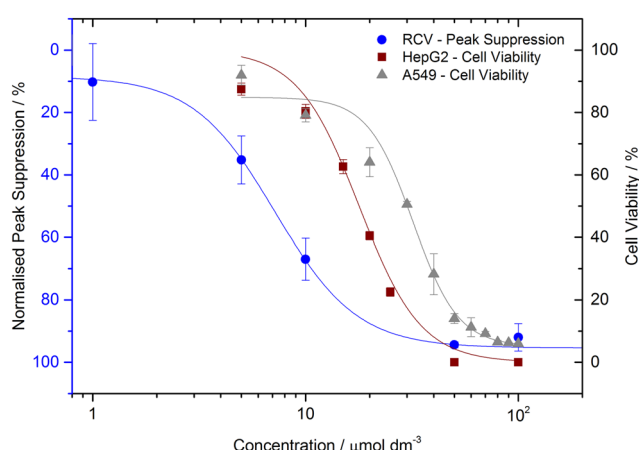


FIG. 8. Normalized percentage suppression of the first capacitance–current peak observed on the forward scan of RCV measurements compared against cell viability studies of HepG2 and A549 cells after interaction with chlorpromazine.

where h is the peak suppression (%), h_{∞} is the peak suppression at the highest concentration (%), h_0 is the initial peak suppression at the lowest concentration (%), c is the concentration of the biomembrane-active sample ($\mu\text{mol dm}^{-3}$), EC_{50} is the concentration resulting in a response half way between h_0 and h_{∞} ($\mu\text{mol dm}^{-3}$), and n is a factor that determines the gradient of the curve. All parameters determined from the sigmoidal fit for the dose response curves in Fig. 8 are compared in the [supplementary material](#). The EC_{50} measured for the RCV platform using this fit was $7.2 \mu\text{mol dm}^{-3}$, while the HepG2 and A549 cell lines gave EC_{50} values of $17 \mu\text{mol dm}^{-3}$ and

$32 \mu\text{mol dm}^{-3}$, respectively. Broeders *et al.*⁵³ also completed cytotoxicity studies of chlorpromazine interaction with human intestinal, human liver, and murine fibroblast cell lines and similarly reported EC_{50} values in the range of $7\text{--}70 \mu\text{mol dm}^{-3}$, dependent on the cell line. The phospholipid monolayer sensing technique represents a simplified mimic of a much more complex biological cell structure; therefore, some differences between the results could be expected. However, exceptional agreement between RCV measurements and cytotoxicity assays was observed. The automated RCV platform, however, achieved the same results in approximately 5 min, compared to 24 h required for the cytotoxicity assay measurements, demonstrating its suitability for robust high-throughput screening.

C. AuNM

To confirm that the new validated screening platform was also effective for its intended purpose of rapid screening of nanomaterials, the AuNM was screened. The RCV scans after the interaction of the AuNM (red line) with a DOPC monolayer (black line) are shown in Fig. 9. All RCV scans are included in the [supplementary material](#). An interaction of the AuNM with the DOPC monolayer was observed at concentrations above $10 \mu\text{mol dm}^{-3}$ of Au in the dispersion. No significant interactions were observed at concentrations lower than this. Suppression of the peaks above $10 \mu\text{mol dm}^{-3}$ was likely caused by the AuNM adsorbing to the DOPC monolayer, suppressing the peaks and potentially influencing the fluidity of the phospholipid layer. Vakurov *et al.*¹⁰ observed similar suppressed RCV peaks after the interaction of silica nanoparticles with a DOPC monolayer, and observed adsorption of the nanoparticles to the DOPC monolayer using SEM. Due to the wide range of properties that nanomaterials can possess, and their subsequent effect

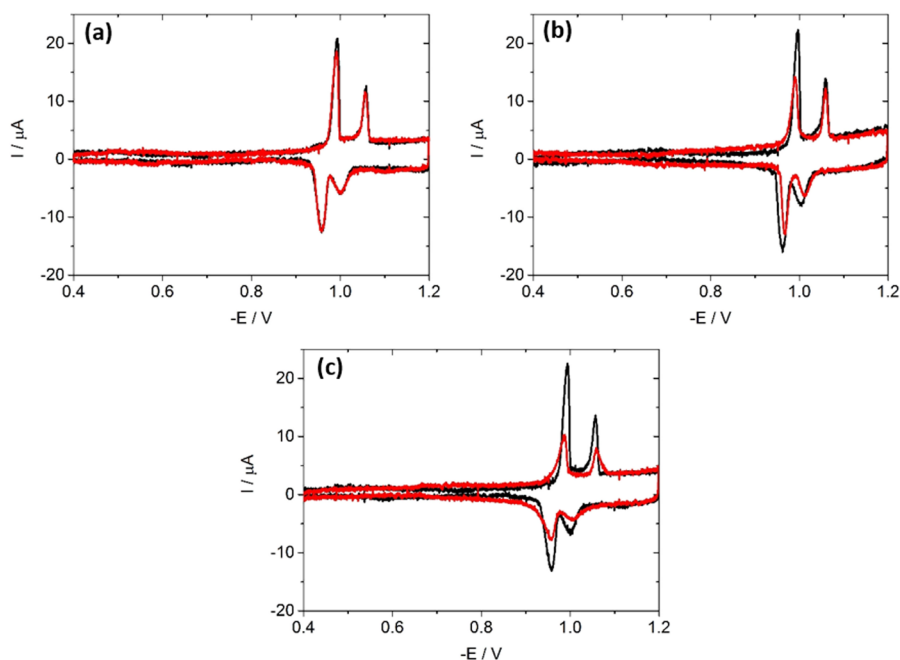


FIG. 9. RCV scans recorded at 40 V s^{-1} of an Hg-supported DOPC monolayer (black line) and interaction with the AuNM (red line) with a Au concentration of (a) $0.001 \mu\text{mol dm}^{-3}$, (b) $50 \mu\text{mol dm}^{-3}$, and (c) $100 \mu\text{mol dm}^{-3}$ in PBS at pH 7.4 (all RCV scans in the [supplementary material](#)).

on cytotoxicity, direct comparison between the monolayer interactions observed in this study with the literature cannot be completed easily. For example, it has been shown for both the AuNM²¹ and the zinc oxide nanomaterial⁵ that differences of particle size or particle coating can significantly influence the severity of membrane interaction. However, the strong agreement between RCV measurements and *in vitro* cytotoxicity assays observed for chlorpromazine in Fig. 8, and a previous study comparing the interaction of silica nanoparticles with the monolayer-on-chip technique and unilamellar vesicles²¹ gives credibility to the biological relevance of the electrochemical results representing membrane interactions observed in Fig. 9.

The percentage peak suppression of the first capacitance–current peak on the forward scan after interaction of the AuNM with the DOPC monolayer is shown in Fig. 10. Average peak heights for each AuNM sample screened (six results for each concentration) are compared against the same baseline DOPC peak height ($19.5 \mu\text{A} \pm 1.4 \mu\text{A}$) used for the chlorpromazine analysis of peak suppression, as shown in Fig. 7. The results from the automated platform were also compared with the results of the AuNM interaction using the older generation, manual system to demonstrate equivalence between the two platforms. The same average DOPC peak baseline ($20.9 \mu\text{A} \pm 1.5 \mu\text{A}$) for chlorpromazine interactions, in Fig. 7, on the manual system was used. The same concentrations of the AuNM were screened using the manual system, with the average of three measurements reported in Fig. 10. Error bars in Fig. 10 for both sets of data represent the standard deviation of the peak suppression measurements. Similar results were obtained for differences between the peak suppressions measured on the automated platform and the manual system, with the average difference between the results measured on both platforms equal to 8% peak suppression.

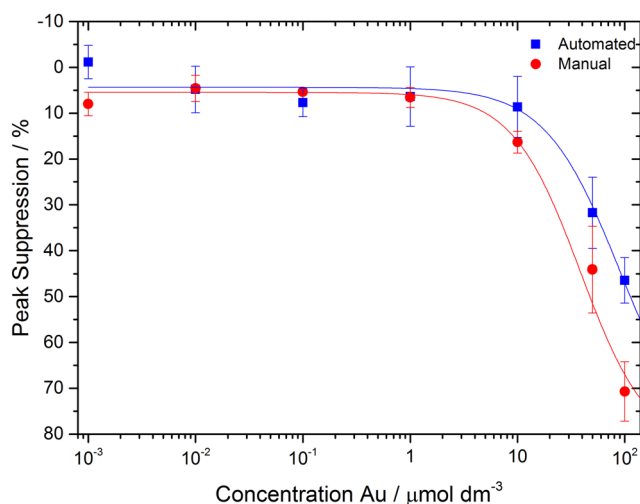


FIG. 10. Percentage suppression of the first capacitance–current peak observed on the forward scan of RCV measurements, at a potential of approximately -0.96 V , after interaction of the AuNM at different concentrations with an Hg-supported DOPC monolayer electrode in PBS at pH 7.4, showing equivalence between the new automated platform and the manual predecessor biomembrane sensing system.

A sigmoidal fit was used for both datasets in Fig. 7, as defined by Eq. (1). Concentrations above $100 \mu\text{mol dm}^{-3}$ could not be screened due to the maximum stock concentration of the AuNM; therefore, a value for h_{∞} was approximated of $82.5\% \pm 7.5\%$ to enable a logistic fit to be determined. This was estimated to be the typical maximum peak suppression possible, determined from the chlorpromazine results in Fig. 7, and RCV responses reported in the literature using the same technique.^{7,10,28,29} A similar trend was observed between the results obtained on the manual system and the results obtained on the automated platform. However, the concentrations of the AuNM for EC_{50} were approximately double on the automated platform ($30 \mu\text{mol dm}^{-3}$) compared to the manual system ($14 \mu\text{mol dm}^{-3}$), potentially as a result of minor differences in the flow cell design influencing the transport of the AuNM to the sensing electrode.

D. Viability of the platform for high-throughput nanomaterial screening

This study has presented a viable solution to rapid, high-throughput *in vitro* solutions for sensing nanomaterial–biomembrane interactions. Some of the main challenges required for nanomaterial screening, such as the requirements for high-throughput and appropriate flow channel designs to allow the required transport of nanomaterials to sensing areas, discussed in Sec. I, have been addressed in the new platform design, improving the potential for a wider usage of the technique for screening nanomaterials. Despite being a phospholipid monolayer system, and therefore being a simplified mimic of a complex cell membrane structure, a strong correlation was observed for chlorpromazine screening on the automated RCV platform and *in vitro* cell viability studies in HepG2 and A549 cells. However, the results on the automated screening platform were obtained in $\sim 5\text{--}6 \text{ min}$ per assay, whereas the cell viability cytotoxicity results were obtained after 24 h, demonstrating the advantage of using the electrochemical platform for rapid screening. Some mechanistic understanding of the interaction was also gained with RCV peak suppression likely to be caused by adsorption of the AuNM to the DOPC monolayer.

The platform is ideally suited for investigations of membrane interaction in a range of experimental conditions. Different cell membrane compositions, for example, can be analyzed through the use of multiple phospholipids, to create a mixed phospholipid membrane monolayer supported on Hg,³⁵ or through the integration of cholesterol into the supported monolayer,³⁴ widening the potential scope of nanomaterial–biomembrane interaction investigations. Limitations of some cytotoxicity assays, such as the possibility of nanomaterial transformations in the assay, as discussed in Sec. I, can also be avoided due to the rapid screening time, enabling a precisely controlled environment for screening nanomaterials.

This work has also demonstrated important improvements to the screening technique, significantly increasing its viability as a high-throughput *in vitro* solution for nanomaterial screening. Throughput was significantly increased, compared to the predecessor system, with the screening time reduced from approximately 10 min per assay to 5–6 min per assay on the new automated platform. Consumption of PBS was also significantly decreased by at least 50%. Stable DOPC monolayers could be formed on the Pt/Hg electrode, confirmed by consistent and durable peak heights, using

only 5 cm^{-3} of DOPC, 50% less than consumed on the manual system, as a result of a smaller sensing volume in the new microfluidic flow cell. This also decreased the quantity of waste fluid from the screening. In addition to decreased fluid consumption, the screening process was carried out with much greater ease using the new platform, due to automation of the system and the development of an easy-to-use user interface. The sensitivity of the electrochemically measured results to flow rates and consumption of DOPC and PBS could also be investigated more thoroughly as a result of automation. Potential also exists to increase throughput and usability further, by automating data processing to quantify biomembrane activity in real-time and increasing the number of sensing modules integrated on to the platform.

V. CONCLUSION

An automated electrochemical biomembrane screening platform has been developed for the purpose of rapid, high-throughput screening of nanomaterial–biomembrane interactions. The design of the platform has been discussed, with chlorpromazine and the AuNM assessed using the screening platform to demonstrate the performance of the system and its viability as a high-throughput sensor for screening nanomaterials. The following conclusions were reached:

- A new screening platform was developed to enhance an existing, well-established technique for sensing biomembrane activity with significantly decreased operator skill level requirements, by automating key aspects of the screening process and integrating automated syringe pumps into the platform design.
- An easy-to-use user interface was developed to control the screening platform and display the electrochemical results, simplifying the screening process.
- Chlorpromazine and the AuNM were screened using the new platform, with both showing interactions with the DOPC membrane at concentrations of greater than $1\text{ }\mu\text{mol dm}^{-3}$.
- A strong correlation was observed between the RCV-measured biomembrane interaction after the interaction of chlorpromazine with the DOPC monolayer and routine *in vitro* cytotoxicity assays.
- Decreased fluid consumption during screening was achieved by decreasing the volume of tubing required to transport fluids to the flow cell, by designing a new microfluidic flow cell and automated syringe pumps to store and control the flow of fluids into the flow cell, decreasing buffer and DOPC usage by approximately 50% compared to the predecessor screening system.
- The screening time was reduced to <6 min per assay, significantly improving throughout the technique.

SUPPLEMENTARY MATERIAL

See the [supplementary material](#) for further detail on the CFD turbulence model used, the user interface developed for the screening platform and for the RCV scans of the AuNM and chlorpromazine at all concentrations screened using the automated platform.

ACKNOWLEDGMENTS

This work was completed as part of the HISENTS program, which has received funding from the European Union's Horizon 2020 research and innovation program under Grant Agreement No. 685817.

REFERENCES

- ¹R. Damoiseaux, S. George, M. Li, S. Pokhrel, Z. Ji, B. France, T. Xia, E. Suarez, R. Rallo, and L. Mädler, "No time to lose—high throughput screening to assess nanomaterial safety," *Nanoscale* **3**(4), 1345–1360 (2011).
- ²M. De, P. S. Ghosh, and V. M. Rotello, "Applications of nanoparticles in biology," *Adv. Mater.* **20**(22), 4225–4241 (2008).
- ³M. Mortimer, K. Kasemets, M. Heinlaan, I. Kurvet, and A. Kahru, "High throughput kinetic *Vibrio fischeri* bioluminescence inhibition assay for study of toxic effects of nanoparticles," *Toxicol. Vitro* **22**(5), 1412–1417 (2008).
- ⁴O. V. Salata, "Applications of nanoparticles in biology and medicine," *J. Nanobiotechnol.* **2**(1), 3 (2004).
- ⁵A. Vakurov, G. Mokry, R. Drummond-Brydson, R. Wallace, C. Svendsen, and A. Nelson, "ZnO nanoparticle interactions with phospholipid monolayers," *J. Colloid Interface Sci.* **404**, 161–168 (2013).
- ⁶W.-T. Liu, "Nanoparticles and their biological and environmental applications," *J. Biosci. Bioeng.* **102**(1), 1–7 (2006).
- ⁷A. Vakurov, R. Drummond-Brydson, O. Ugwumsinachi, and A. Nelson, "Significance of particle size and charge capacity in TiO₂ nanoparticle–lipid interactions," *J. Colloid Interface Sci.* **473**, 75–83 (2016).
- ⁸I. Hansjosten, J. Rapp, L. Reiner, R. Vatter, S. Fritsch-Decker, R. Peravali, T. Palosaari, E. Joossens, K. Gerloff, P. Macko, M. Whelan, D. Gilliland, I. Ojea-Jimenez, M. P. Monopoli, L. Rocks, D. Garry, K. Dawson, P. J. F. Röttgermann, A. Murschhauser, J. O. Rädler, S. V. Y. Tang, P. Gooden, M.-F. A. Belinga-Desaunay, A. O. Khan, S. Briffa, E. Guggenheim, A. Papadiamantis, I. Lynch, E. Valsami-Jones, S. Diabaté, and C. Weiss, "Microscopy-based high-throughput assays enable multi-parametric analysis to assess adverse effects of nanomaterials in various cell lines," *Arch. Toxicol.* **92**(2), 633–649 (2018).
- ⁹A. R. Gliga, S. Skoglund, I. O. Wallinder, B. Fadeel, and H. L. Karlsson, "Size-dependent cytotoxicity of silver nanoparticles in human lung cells: The role of cellular uptake, agglomeration and Ag release," *Part. Fibre Toxicol.* **11**(1), 11 (2014).
- ¹⁰A. Vakurov, R. Brydson, and A. Nelson, "Electrochemical modeling of the silica nanoparticle–biomembrane interaction," *Langmuir* **28**(2), 1246–1255 (2011).
- ¹¹N. Lewinski, V. Colvin, and R. Drezek, "Cytotoxicity of nanoparticles," *Small* **4**(1), 26–49 (2008).
- ¹²C. Lopez-Chaves, J. Soto-Alvaredo, M. Montes-Bayon, J. Bettmer, J. Llopis, and C. Sanchez-Gonzalez, "Gold nanoparticles: Distribution, bioaccumulation and toxicity. *In vitro* and *in vivo* studies," *Nanomaterials*, *Nanotechnol., Biol. Med.* **14**(1), 1–12 (2018).
- ¹³A. Nel, T. Xia, H. Meng, X. Wang, S. Lin, Z. Ji, and H. Zhang, "Nanomaterial toxicity testing in the 21st century: Use of a predictive toxicological approach and high-throughput screening," *Acc. Chem. Res.* **46**(3), 607–621 (2012).
- ¹⁴S. George, T. Xia, R. Rallo, Y. Zhao, Z. Ji, S. Lin, X. Wang, H. Zhang, B. France, and D. Schoenfeld, "Use of a high-throughput screening approach coupled with *in vivo* zebrafish embryo screening to develop hazard ranking for engineered nanomaterials," *ACS Nano* **5**(3), 1805–1817 (2011).
- ¹⁵A. Astashkina, B. Mann, and D. W. Grainger, "A critical evaluation of *in vitro* cell culture models for high-throughput drug screening and toxicity," *Pharmacol. Ther.* **134**(1), 82–106 (2012).
- ¹⁶S. K. Mahto, V. Charwat, P. Ertl, B. Rothen-Rutishauser, S. W. Rhee, and J. Sznitman, "Microfluidic platforms for advanced risk assessments of nanomaterials," *Nanotoxicology* **9**(3), 381–395 (2015).
- ¹⁷A. Verma and F. Stellacci, "Effect of surface properties on nanoparticle–cell interactions," *Small* **6**(1), 12–21 (2010).
- ¹⁸A. H. Churchman, R. Wallace, S. J. Milne, A. P. Brown, R. Brydson, and P. A. Beales, "Serum albumin enhances the membrane activity of ZnO nanoparticles," *Chem. Commun.* **49**(39), 4172–4174 (2013).

- ¹⁹P. R. Leroueil, S. Hong, A. Mecke, J. R. Baker, Jr., B. G. Orr, and M. M. Banaszak Holl, "Nanoparticle interaction with biological membranes: Does nanotechnology present a Janus face?," *Acc. Chem. Res.* **40**(5), 335–342 (2007).
- ²⁰Q. Mu, C. A. David, J. Galceran, C. Rey-Castro, L. Krzemiński, R. Wallace, F. Bamiduro, S. J. Milne, N. S. Hondow, and R. Brydson, "Systematic investigation of the physicochemical factors that contribute to the toxicity of ZnO nanoparticles," *Chem. Res. Toxicol.* **27**(4), 558–567 (2014).
- ²¹S. Zhang, A. Nelson, and P. A. Beales, "Freezing or wrapping: The role of particle size in the mechanism of nanoparticle–biomembrane interaction," *Langmuir* **28**(35), 12831–12837 (2012).
- ²²C. F. Jones and D. W. Grainger, "In vitro assessments of nanomaterial toxicity," *Adv. Drug Delivery Rev.* **61**(6), 438–456 (2009).
- ²³S. George, S. Pokhrel, T. Xia, B. Gilbert, Z. Ji, M. Schowalter, A. Rosenauer, R. Damoiseaux, K. A. Bradley, and L. Mädler, "Use of a rapid cytotoxicity screening approach to engineer a safer zinc oxide nanoparticle through iron doping," *ACS Nano* **4**(1), 15–29 (2009).
- ²⁴A. R. Collins, B. Annangi, L. Rubio, R. Marcos, M. Dorn, C. Merker, I. Estrela-Lopis, M. R. Cimpan, M. Ibrahim, and E. Cimpan, "High throughput toxicity screening and intracellular detection of nanomaterials," *Wiley Interdiscip. Rev.: Nanomed. Nanobiotechnol.* **9**(1), e1413 (2017).
- ²⁵Z. Coldrick, A. Penezić, B. Gašparović, P. Steenson, J. Merrifield, and A. Nelson, "High throughput systems for screening biomembrane interactions on fabricated mercury film electrodes," *J. Appl. Electrochem.* **41**(8), 939–949 (2011).
- ²⁶Z. Coldrick, P. Steenson, P. Millner, M. Davies, and A. Nelson, "Phospholipid monolayer coated microfabricated electrodes to model the interaction of molecules with biomembranes," *Electrochim. Acta* **54**(22), 4954–4962 (2009).
- ²⁷I. Miller, J. Rishpon, and A. Tenenbaum, "Electrochemical determination of structure and interactions in spread lipid monolayers," *Bioelectrochem. Bioenerg.* **3**(3–4), 528–542 (1976).
- ²⁸A. Nelson, "Penetration of mercury-adsorbed phospholipid monolayers by polynuclear aromatic hydrocarbons," *Anal. Chim. Acta* **194**, 139–149 (1987).
- ²⁹A. Nelson, N. Auffret, and J. Borlakoglu, "Interaction of hydrophobic organic compounds with mercury adsorbed dioleoylphosphatidylcholine monolayers," *Biochim. Biophys. Acta, Biomembr.* **1021**(2), 205–216 (1990).
- ³⁰A. Nelson, N. Auffret, and J. Readman, "Initial applications of phospholipid-coated mercury electrodes to the determination of polynuclear aromatic hydrocarbons and other organic micropollutants in aqueous systems," *Anal. Chim. Acta* **207**, 47–57 (1988).
- ³¹A. Nelson and A. Benton, "Phospholipid monolayers at the mercury/water interface," *J. Electroanal. Chem. Interfacial Electrochem.* **202**(1–2), 253–270 (1986).
- ³²A. Rashid, A. Vakurov, S. Mohamadi, D. Sanver, and A. Nelson, "Substituents modulate biphenyl penetration into lipid membranes," *Biochim. Biophys. Acta, Biomembr.* **1859**(5), 712–721 (2017).
- ³³A. Rashid, A. Vakurov, and A. Nelson, "Role of electrolyte in the occurrence of the voltage induced phase transitions in a dioleoyl phosphatidylcholine monolayer on Hg," *Electrochim. Acta* **155**, 458–465 (2015).
- ³⁴A. Nelson and N. Auffret, "Phospholipid monolayers of di-oleoyl lecithin at the mercury/water interface," *J. Electroanal. Chem. Interfacial Electrochem.* **244**(1–2), 99–113 (1988).
- ³⁵F. Neville, D. Gidalevitz, G. Kale, and A. Nelson, "Electrochemical screening of anti-microbial peptide LL-37 interaction with phospholipids," *Bioelectrochem. Bioenerg.* **70**(2), 205–213 (2007).
- ³⁶L. Ringstad, E. Protopapa, B. Lindholm-Sethson, A. Schmidtchen, A. Nelson, and M. Malmsten, "An electrochemical study into the interaction between complement-derived peptides and DOPC mono- and bilayers," *Langmuir* **24**(1), 208–216 (2008).
- ³⁷B. Drasler, P. Sayre, K. G. Steinhäuser, A. Petri-Fink, and B. Rothen-Rutishauser, "In vitro approaches to assess the hazard of nanomaterials," *Nanolm-pact* **8**, 99–116 (2017).
- ³⁸R. Guadagnini, B. Halamoda Kenzaoui, L. Walker, G. Pojana, Z. Magdolenova, D. Bilanovic, M. Saunders, L. Juillerat-Jeanneret, A. Marcomini, and A. Huk, "Toxicity screenings of nanomaterials: Challenges due to interference with assay processes and components of classic in vitro tests," *Nanotoxicology* **9**(sup1), 13–24 (2015).
- ³⁹A. Kroll, M. H. Pillukat, D. Hahn, and J. Schneckeburger, "Current in vitro methods in nanoparticle risk assessment: Limitations and challenges," *Eur. J. Pharm. Biopharm.* **72**(2), 370–377 (2009).
- ⁴⁰A. Nelson, "Electrochemistry of mercury supported phospholipid monolayers and bilayers," *Curr. Opin. Colloid Interface Sci.* **15**(6), 455–466 (2010).
- ⁴¹G. Du, Q. Fang, and J. M. den Toonder, "Microfluidics for cell-based high throughput screening platforms—A review," *Anal. Chim. Acta* **903**, 36–50 (2016).
- ⁴²Á. Ríos, M. Zougagh, and M. Avila, "Miniaturization through lab-on-a-chip: Utopia or reality for routine laboratories? A review," *Anal. Chim. Acta* **740**, 1–11 (2012).
- ⁴³G. M. Whitesides, "The origins and the future of microfluidics," *Nature* **442**(7101), 368 (2006).
- ⁴⁴E. K. Sackmann, A. L. Fulton, and D. J. Beebe, "The present and future role of microfluidics in biomedical research," *Nature* **507**(7491), 181 (2014).
- ⁴⁵B. Nasser, N. Soleimani, N. Rabiee, A. Kalbasi, M. Karimi, and M. R. Hamblin, "Point-of-care microfluidic devices for pathogen detection," *Biosens. Bioelectron.* **117**, 112 (2018).
- ⁴⁶J. Zhang, S. Yan, D. Yuan, G. Alici, N.-T. Nguyen, M. E. Warkiani, and W. Li, "Fundamentals and applications of inertial microfluidics: A review," *Lab Chip* **16**(1), 10–34 (2016).
- ⁴⁷P. M. Valencia, O. C. Farokhzad, R. Karnik, and R. Langer, "Microfluidic technologies for accelerating the clinical translation of nanoparticles," *Nat. Nanotechnol.* **7**(10), 623 (2012).
- ⁴⁸D. Pike, N. Kapur, P. Millner, and D. Stewart, "Flow cell design for effective biosensing," *Sensors* **13**(1), 58–70 (2013).
- ⁴⁹R. Barker, B. Pickles, N. Kapur, T. Hughes, E. Barmatov, and A. Neville, "Flow cell apparatus for quantitative evaluation of carbon steel corrosion during transitions in fluid composition: Application to transition from inhibited hydrochloric acid to sodium chloride brine," *Corros. Sci.* **138**, 116–129 (2018).
- ⁵⁰COMSOL Multiphysics v5.3a Chemical Reaction Engineering Module User's Guide, 2017.
- ⁵¹L. Y. Rizzo, S. K. Golombek, M. E. Mertens, Y. Pan, D. Laaf, J. Broda, J. Jayapaul, D. Möckel, V. Subr, and W. E. Hennink, "In vivo nanotoxicity testing using the zebrafish embryo assay," *J. Mater. Chem. B* **1**(32), 3918–3925 (2013).
- ⁵²A. DeLean, P. Munson, and D. Rodbard, "Simultaneous analysis of families of sigmoidal curves: Application to bioassay, radioligand assay, and physiological dose-response curves," *Am. J. Physiology* **235**(2), E97 (1978).
- ⁵³J. J. Broeders, B. J. Blaauw, and J. L. Hermens, "In vitro biokinetics of chlorpromazine and the influence of different dose metrics on effect concentrations for cytotoxicity in Balb/c 3T3, Caco-2 and HepaRG cell cultures," *Toxicol. Vitro* **27**(3), 1057–1064 (2013).